ARTICLE

Check for updates

Maturation-dependent changes in the size, structure and seeding capacity of Aβ42 amyloid fibrils

Alyssa Miller[1], Sean Chia[1], Ewa Klimont[1], Tuomas P. J. Knowles [1,2✉], Michele Vendruscolo [1✉] & Francesco Simone Ruggeri [3,4✉]

Many proteins self-assemble to form amyloid fibrils, which are highly organized structures stabilized by a characteristic cross-β network of hydrogen bonds. This process underlies a variety of human diseases and can be exploited to develop versatile functional biomaterials. Thus, protein self-assembly has been widely studied to shed light on the properties of fibrils and their intermediates. A still open question in the field concerns the microscopic processes that underlie the long-time behaviour and properties of amyloid fibrillar assemblies. Here, we use atomic force microscopy with angstrom-sensitivity to observe that amyloid fibrils undergo a maturation process, associated with an increase in both fibril length and thickness, leading to a decrease of their density, and to a change in their cross-β sheet content. These changes affect the ability of the fibrils to catalyse the formation of new aggregates. The identification of these changes helps us understand the fibril maturation processes, facilitate the targeting of amyloid fibrils in drug discovery, and offer insight into the development of biocompatible and sustainable protein-based materials.

[1] Yusuf Hamied Department of Chemistry, University of Cambridge, Lensfield Road, Cambridge CB2 1EW, UK. [2] Cavendish Laboratory, University of Cambridge, Cambridge CB3 0HE, UK. [3] Laboratory of Organic Chemistry, Wageningen University & Research, Stippeneng 4, Wageningen 6703 WE, the Netherlands. [4] Physical Chemistry and Soft Matter, Wageningen University & Research, Wageningen University, Stippeneng 4, Wageningen 6703 WE, the Netherlands. ✉email: tpjk2@cam.ac.uk; mv245@cam.ac.uk; simone.ruggeri@wur.nl

The study of protein aggregation and amyloid formation has gained attention over the past few decades because of its association with human disease, such as in the case of the amyloid-β peptide (Aβ) in Alzheimer's disease (AD). The process of supramolecular aggregation involves the conversion of soluble monomers into large, insoluble, cross-β amyloid fibrils, which possess an extended, highly ordered network of intermolecular hydrogen bonding[1]. When monitored in vitro using assays that report on the mass of aggregates structures present, the process of aggregation characteristically involves three phases: (1) a lag phase, where initial aggregates form but their numbers are below the detection threshold[2], (2) a growth phase, where the aggregates proliferate rapidly, and (3) a plateau phase, where the bulk aggregate mass stops increasing because all the supersaturated monomers have been used up[3].

At a single-molecule scale, this macroscopic behaviour can be explained by a complex network of microscopic processes. These processes have been investigated through the development of reproducible aggregation reactions in vitro, which can be monitored via fluorescent probes for cross-β sheet structures, such as thioflavin T (ThT), and the development of analytical methods to extract kinetic information from bulk data[4–7]. These analytical approaches have provided key mechanistic insights into the fast processes of aggregation, revealing that the most important microscopic processes, at least during the lag and growth phases, include: (1) primary nucleation, where initial fibril seeds are formed, (2) elongation, where the seeds grow into fibrils, (3) secondary nucleation, where existing fibrils catalyse the formation of new seeds, and (4) fragmentation, where fibrils break to generate new growing ends. Since secondary nucleation and fragmentation of mature fibrillar aggregates, collectively referred to as secondary processes, are mainly responsible for the proliferation of the aggregates, it is important to study them in detail[6].

The plateau phase can provide a wealth of information about the role of fibrils in secondary processes. However, it has been challenging to obtain mechanistic information about the plateau phase when using standard fluorescent probes. Bulk techniques, such as ThT-fluorescence, provide useful information on the average properties of fibrils in solution. However, their use does not readily capture the subtle changes in heterogeneity characteristic of protein self-assembly processes. Thus, this approach leaves a gap between the in vitro study of fibril assembly and the formation of supramolecular fibril assemblies that make up amyloid plaques and inclusions in disease tissues.

Traditional structural methods, such as cryo-electron microscopy (cryo-EM) and nuclear magnetic resonance (NMR) spectroscopy, have provided atomistic descriptions of the core structure of amyloid fibrils[8–10]. However, it can be difficult to extend these techniques to capture the full breadth of heterogeneity of amyloid fibrils due to averaging effects. Therefore, to investigate fibrils in the plateau phase, one can exploit both bulk methods and single-molecule methods to obtain a more complete picture of the time evolution of the aggregates. Atomic force microscopy (AFM) is a single molecule technique that can be used to measure the time-resolved 3D structural properties of amyloid assemblies at the single-fibril level[11]. However, preparing studies for complementary bulk techniques can be challenging due to the different conditions required by these experiments. For example, bulk aggregation reactions carried out in plate readers are carried out with much lower concentrations of proteins than needed for a bulk infrared (IR) spectroscopy measurements. This makes it impractical to perform parallel studies of multiple fibrillar properties.

Here, we address the problem of identifying the microscopic changes in amyloid fibrils that take place during the plateau phase. Our results illustrate changes in morphology, size and structure of heterogeneous, mature Aβ42 fibrils in this phase. We report on the properties of fibrillar aggregates of Aβ42 as a function of time during the early hours of the plateau phase, where ThT fluorescence intensity remains constant. We analyse in vitro aggregation experiments by using a combination of single-molecule AFM imaging, Fourier transform infrared (FTIR) spectroscopy, chemical kinetics (Fig. 1), and a microfluidic deposition[12–14]. Using bulk and single-molecule approaches, we characterize changes in the fibrillar size and structure during the plateau phase. This information enables investigations of both seeding and secondary processes, which facilitate the development of compounds targeting amyloid aggregates for pharmacological interventions. This approach also provides a framework to study the structure of protein nanofibrils which can be useful to produce functional biomaterials.

Results and discussion

To characterise the properties of fibrillar aggregates in the plateau phase, we first monitored the aggregation of Aβ42 monomers using a ThT-kinetics based assay (Fig. 2). We defined the beginning of the plateau phase as the region where the growth curve approached a slope of zero. We first assessed the ability of fibrils to act as effective templates for conversion of monomers into aggregates, i.e. the seeding capacity, as a function of time. We thus took aliquots from an ongoing reaction at the start of the plateau phase (0 h, early), and after few hours (4 h, late), and used these aliquots to generate fibril seeds. These seeds were then reintroduced to monomer solutions, where they acted as templates for self-assembly (Fig. 2).

We found that the dominant aggregation mechanism in the presence of seeds was secondary nucleation, as is typical for Aβ42 (Fig. S1)[6]. The aggregation of Aβ42 was accelerated in the presence of fibril seeds as compared to its absence, suggesting that seeds generated from both early and later time points were seeding-competent, promoting conversion of monomers into on-pathway amyloid aggregates. In particular, a difference in seeding ability between the fibrils from early and late time points in the plateau phase was observed at different concentrations of seeds, with the exception of the lowest concentration performed (0.5%), where the difference was much less pronounced. We observed that seeds taken from an earlier timepoint acted as more efficient templates for aggregation, speeding up the kinetics of aggregation.

In order to assess whether the contribution to seeding capacity was due to a difference in fibril mass, we measured the aggregate mass taken at each time point in the plateau phase. This was achieved by measuring the fluorescence intensity of the seeding stocks at the initial time point of the aggregation assays (Fig. S2), as ThT intensity is a readout on the total cross-β sheet mass. The two seeding stocks showed approximately the same intensity, indicating the enhanced seeding capacity of early fibrils is not due to a difference in fibril mass between the two seeding stocks.

Therefore, to quantify this increase in seeding capability, we measured the half-time ($t_{1/2}$) of the aggregation reaction. In the conditions studied here, aggregation reactions with early seeds on average had half times approximately 10–20% shorter than those with late seeds (Fig. 2e). Indeed, in both cases of fibril seeds from early and late time points, the half-times were found to be approximately linearly dependent on the logarithm of the seed concentration (Fig. 2e inset). This suggests a consistent self-seeding behaviour in the presence of secondary pathways for Aβ42 in both cases of seeds[15].

To investigate the structural basis for this change in seeding capacity, we performed phase-controlled single-molecule AFM studies. This approach enables the characterisation of the morphological changes at the single fibril-level (Figs. 2f, 3 and
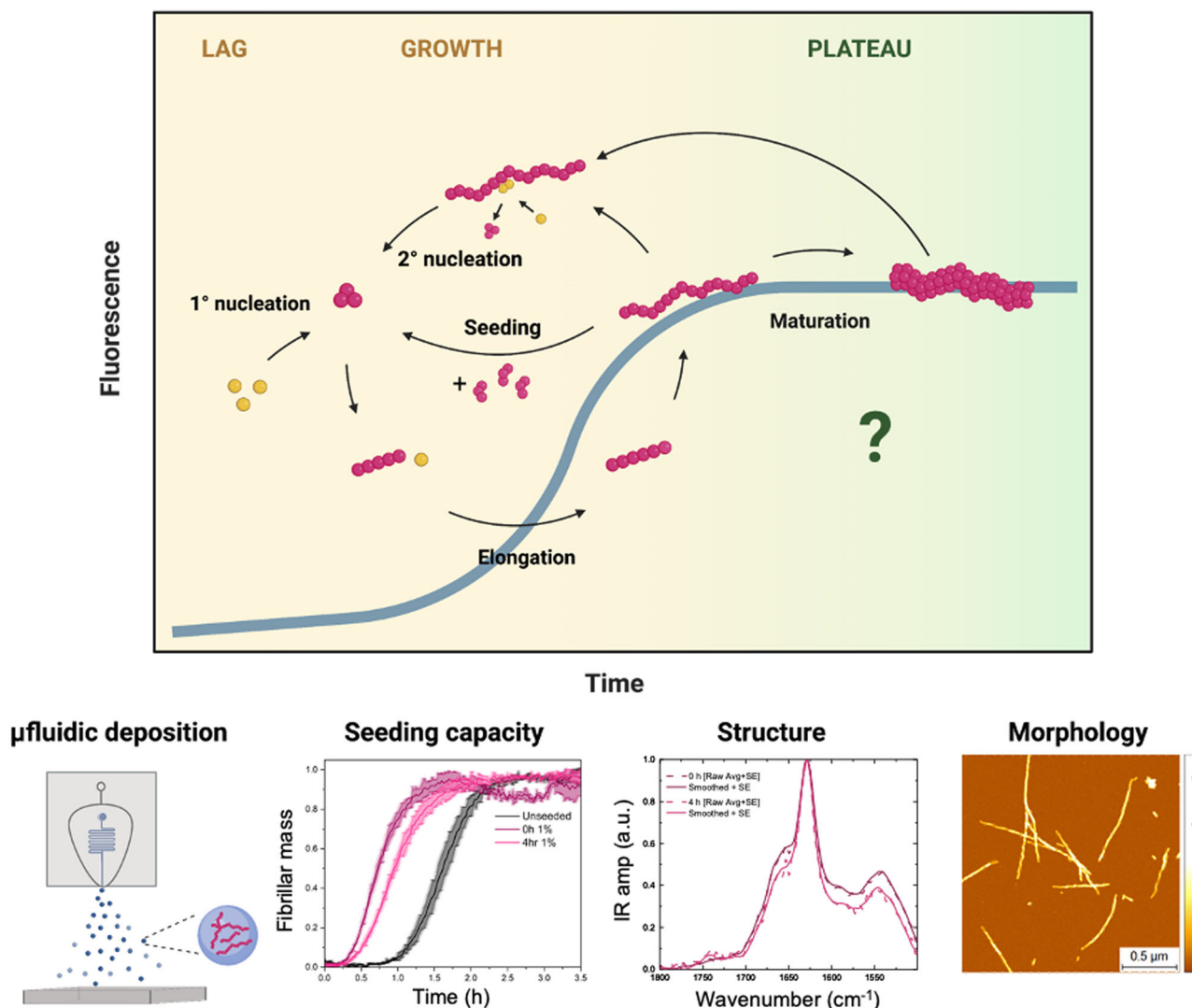
Fig. 1 Unravelling Aβ42 fibrils' morphology and structural changes within the plateau phase. The aggregation of Aβ42 with a schematic of the dominant molecular mechanisms involved was monitored using a ThT-fluorescence assay, sensitive to cross-β formation. Here, using microfluidic sample deposition, we characterise maturation processes of fibrils in the plateau phase by studying dynamic structural features by AFM and FTIR.

Fig. S3). We took aliquots from an ongoing aggregation reaction at early (0 h) and late (4 h) time points within the plateau phase, as above, and immediately deposited the sample onto a mica surface (**3a,b**). We thus acquired phase-controlled maps of the 3D morphology changes of the fibrillar aggregates between the early and late time points of the plateau phase. We could directly measure and quantify an increase in the length, cross-sectional diameter and surface to volume ratio of the fibrils as a function of time in the plateau phase (Fig. 3e, f) by performing a single molecule statistical analysis. Between early and late time points, the average length of fibrillar aggregates increased from 250 ± 25 nm to 330 ± 25 nm. We also measured the average cross-sectional height of fibrillar aggregates, which increased from 5.15 ± 0.25 nm to 5.90 ± 0.30 nm. The increase in size of the fibrillar aggregates corresponded accordingly to a decrease of their density in number on the surface, as observed in Fig. 3c, d.

Overall, the increase of length of the fibrils is consistent with the continual addition of monomers to the fibril ends over time in the plateau phase. In addition, the increase in the cross-sectional diameter (thickness) of fibrils over time in the plateau phase can be attributed to a hierarchical fibril maturation process, in which single protofibril strands and mature fibrils laterally associate with each other to form higher order structures, resulting in a maturation of the cross-β structure[8,16,17]. We also considered whether these observed changes in fibril morphology could be due to the adsorption of monomers or small oligomers to the fibril surface. Most fibrils measured via high-resolution AFM imaging do not show evidence of monomer/small oligomer adsorption. This is demonstrated by the defined fibril twists which are observed, which would be obscured by the presence of small aggregates adsorbed to the surface (Fig. S4). However, we do observe rare instances of monomer/small oligomer adsorption to fibril surfaces (Fig. S5), which is consistent with secondary nucleation processes taking place on fibril surfaces, as described above. We quantified the occurrence of these adsorption events on fibril surfaces by considering the surface area of monomers and oligomers per surface area of fibril, for individual fibrils, and found it to be ~2% for both early and late time points. Also of note, the observed fibril structure changes observed through AFM do not appear to affect the ThT fluorescence signal significantly, as a plateau phase is reached in both early and later seed conditions. This highlights the importance of single-molecule techniques in resolving dynamic structural features of fibrils.
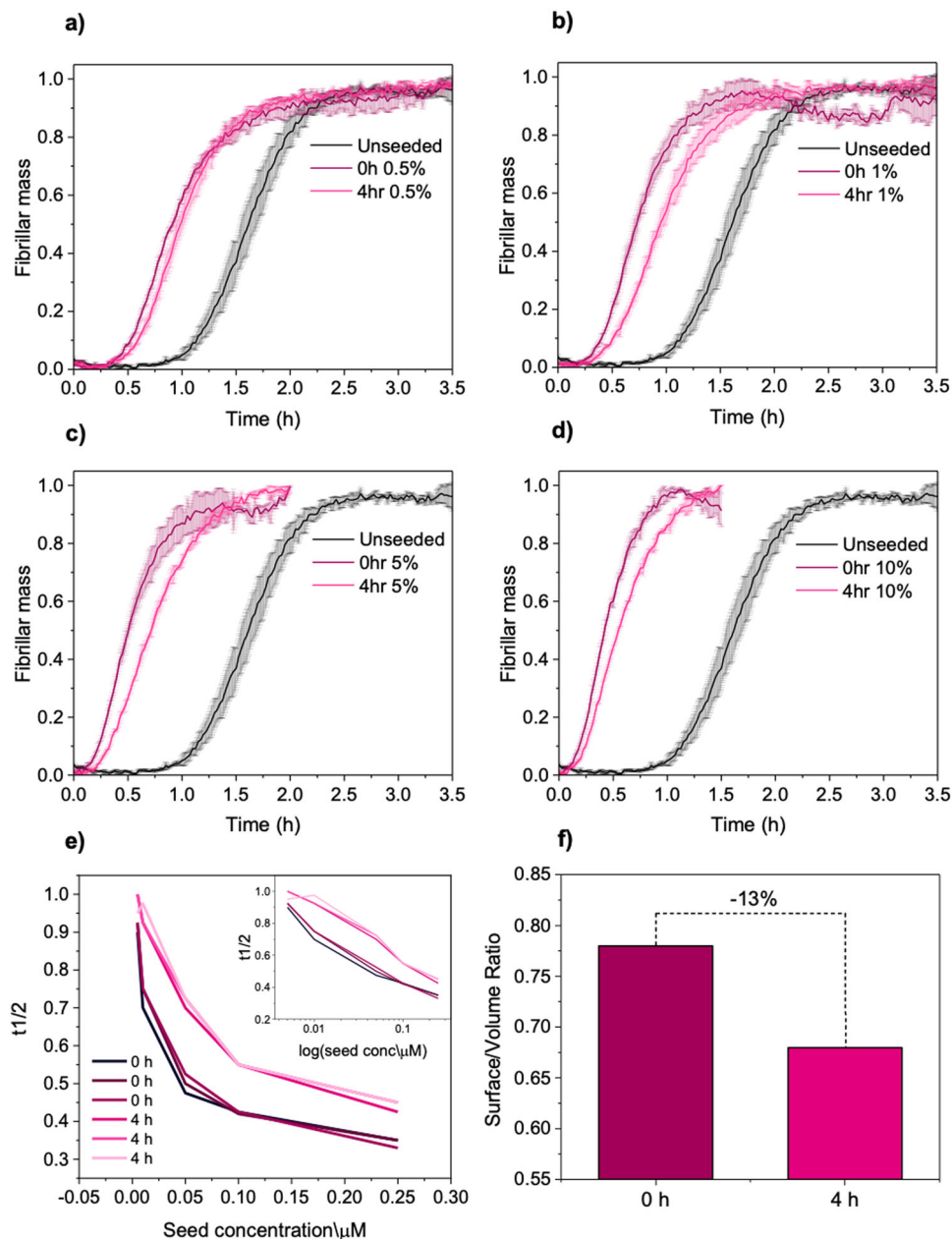
Fig. 2 Seeding capacity of Aβ42 fibrils from different time-points in the plateau phase. a–d Aβ42 seeds were generated from fibrils in the plateau phase at 0 and 4 h, and the kinetic profiles (average and standard deviation, $n = 3$ technical replicates) were compared to unseeded aggregation. Seed concentrations of 0.5% (**a**), 1% (**b**), 5% (**c**) and 10% (**d**) were assessed. **e** The half-time of the aggregation reaction was plotted as a function of seed concentration. The inset shows the data plotted on a logarithmic scale. Seeds generated from fibrils generated later in the plateau phase exhibit a decreased seeding capacity of 20 ± 10%. **f** The surface-to-volume ratio as measured by single fibril imaging decreases by ca. 15% later time points in the plateau phase.

Structural and chemical changes have been reported during the progression from the protofibril to the mature fibril level for a variety of protein systems, which can be affected by aggregation-enhancing mutations[18–23]. However, it has not yet been addressed in the literature if the process of fibril maturation is associated with structural changes at the chemical level[24,25]. Therefore, we next sought to address if the seeding capability and morphological changes of the fibrillar aggregates is associated with changes in the secondary structure, as measured via FTIR.

To facilitate comparisons between aggregates measured via AFM, we performed FTIR measurements in the same conditions (Fig. 4), namely protein concentration (<5 μM) and buffer environment (20 mM sodium phosphate). These conditions

typically represent a problem for FTIR measurements in attenuated total reflection (ATR), as the presence of salt crystals causes spectral distortion for samples with lower protein concentration, preventing us from performing spectral analysis in relevant conditions[14].

As such, we deposited the sample onto the FTIR prism via microfluidic spray deposition (Fig. 4a and Fig. S6)[12–14]. This method minimises salt crystallisation, via ultra-fast droplet drying, to improve the spectroscopic sensitivity such that we were able to acquire spectra with only ~8.3 ng of protein deposited on the prism (Fig. S7). This enabled us to measure IR spectra at relevant buffer and concentration conditions (Fig. 4b), without needing to concentrate the sample, which may mask subtle
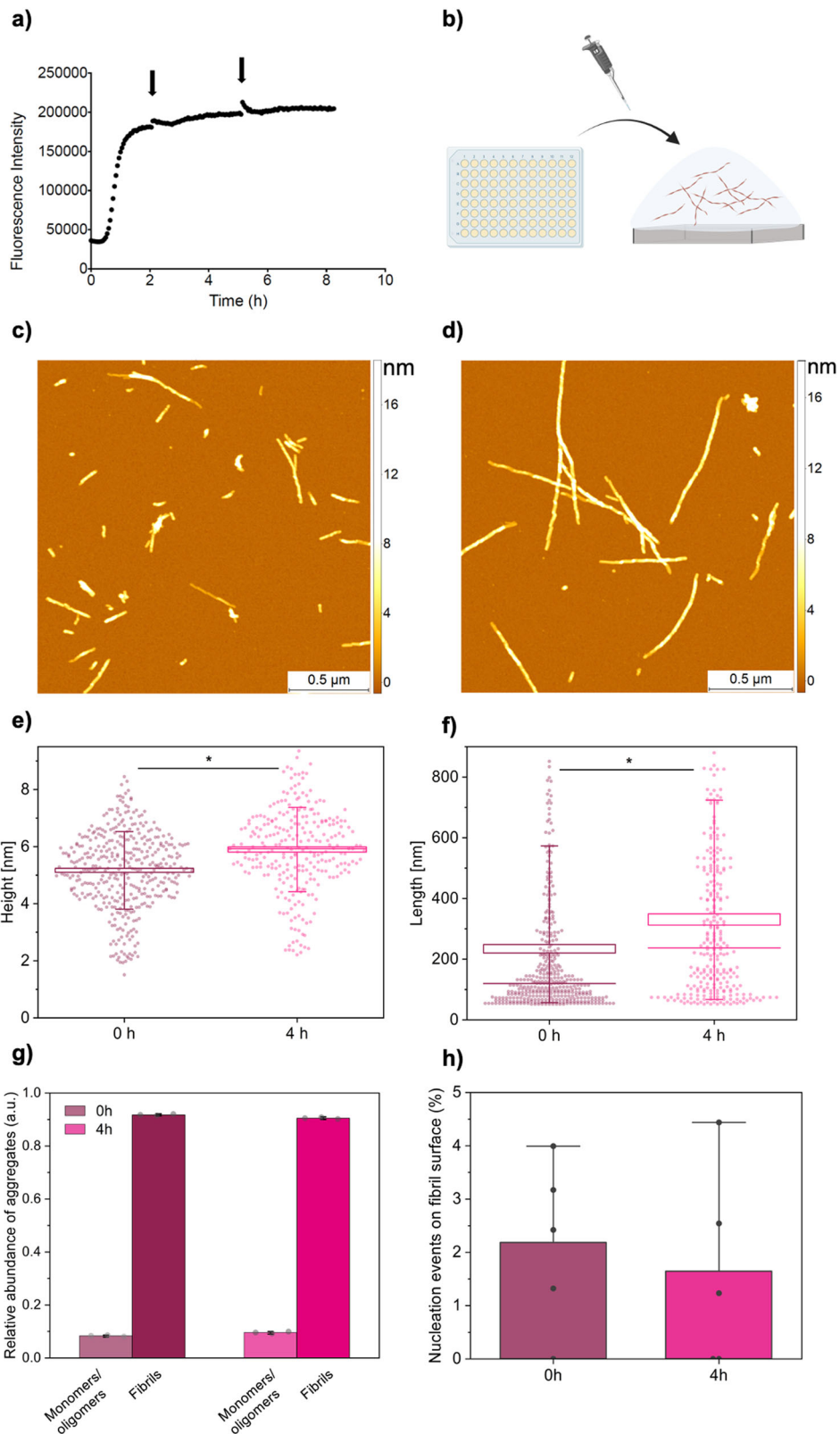
changes between samples at different time points measured in bulk, while also maintaining the full heterogeneity of the sample[14]. This also allowed us to obtain measurements consistent to ThT fluorescence and AFM experiments. Then, we used the information in the IR spectra, we assessed the secondary and quaternary structure of the protein aggregates via the analysis of their amide I peak, which contains information on the type of protein fold present[26]. Using this approach, we measured the secondary structure of fibrillar aggregates taken from an aggregation reaction at early (0 h) and later (4 and 8 h) time points into the plateau phase. At both time points, the spectra showed the characteristic signature of amyloid fibrils cross-β sheet structure at $1628\ cm^{-1}$ (parallel) and $1695\ cm^{-1}$ (antiparallel) (Fig. 4c). We also observe the presence of a random coil/α-helix signature at

Fig. 3 The morphology of Aβ42 fibrils change over time in the plateau phase. a, b Aβ42 fibril formation was monitored using ThT fluorescence, with samples taken from ongoing aggregation reactions (indicated by black arrows) in a 96-well plate, before being deposited on a mica surface. **c, d** Aβ42 fibrils were imaged via AFM at the start of the plateau phase (**c**) and 4 h later (**d**). **e, f** The height (**e**) and length (**f**) of the aggregates were measured for these time points and found to increase over time. Boxes represent ±1 standard error of the mean, lines represent the median, and the whiskers represent the standard deviation. $n = 389$ and 271 for 0 and 4 h, respectively. A one-sided t-test was performed. **g** The relative volume of monomers and small oligomers, measured from AFM maps, is ~8% and 9% at 0 h and 4 h, respectively ($n = 3$ images per time point). Analysis procedure is shown in Fig. S8. **h** Occurrence of monomers and small oligomers were observed on the surface of fibrils. The rate of occurrence of monomers and small oligomers observed on the surface of fibrils was measured by considering the surface area of small aggregates per surface area of fibril for individual fibrils ($n = 5$ for each time point, Fig. S5).
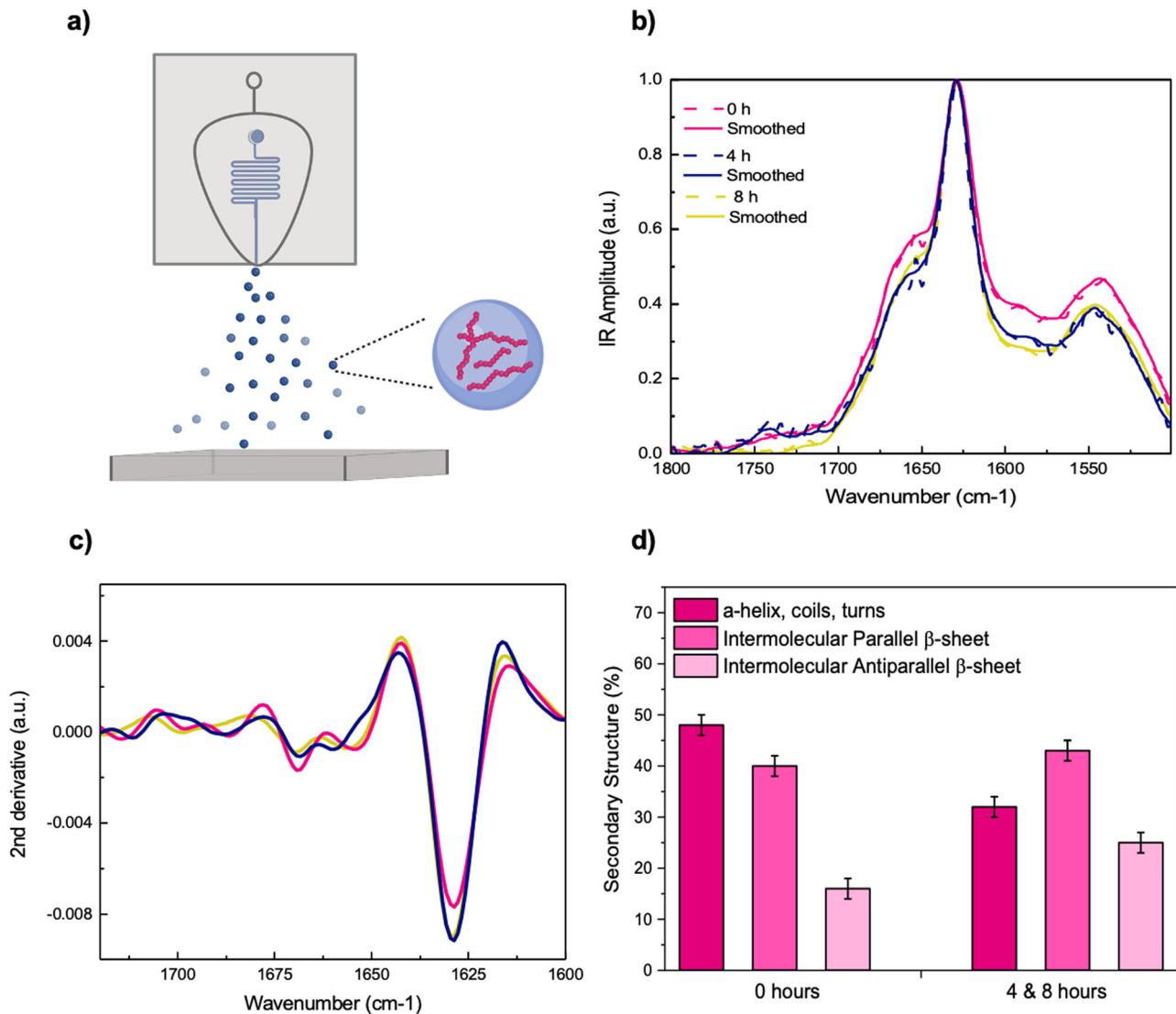

Fig. 4 The secondary structure of Aβ42 fibrils, as monitored by FTIR, indicates a net increase in cross-βstructure over time. a A schematic of the microfluidic spray sample deposition onto the FTIR prism. **b** Fibrils were taken at 0, 4, and 8 h into the plateau phase and deposited directly onto the ATR prism in triplicates (technical replicates). Infrared (IR) spectra were acquired and averaged for all times points. **c** The second derivative was taken for the spectra, revealing a major absorption peak at 1628 cm^{-1}, attributed to intermolecular β-sheet. The cross-β signature is more prominent at 4 and 8 h. **d** Secondary structure components are shown for fibrils at 0, 4, and 8 h in the plateau phase. Error bars represent ±1 SD.

1654 cm^{-1} for both time points, which has been observed for a variety of amyloid assemblies[27–30]. At the early time point, the spectra showed a total cross-β sheet structure of 55 ± 2%, while at the late time points, there is a net increase in this cross-β signature to 69 ± 2% (Fig. 4d), as calculated by band integration and the second derivative analysis of the amide I peak[26].

As FTIR is a bulk technique, we sought to understand the contribution of the observed structural changes coming from the

fibrils versus monomers and small oligomers in the aggregation mixture. Therefore, we measured the relative volumes of aggregate species via analysis of AFM images. We found that monomers/oligomers accounts for 9% and 8% of species at early and late time points, respectively (Fig. 3g and Fig. S8). We note that the AFM tip diameter is much larger than the diameter of these smaller species, resulting in an over-estimation of the volume of small monomers/oligomers. Therefore, the measured change in

secondary structure can be attributed to structural changes of the fibrils, rather than differing levels of smaller aggregate species at the different time points.

The changes in secondary and quaternary structure as a function of the time in the plateau phase, and in particular the increase in cross-β structure content, is consistent with an increase in the density of intermolecular hydrogen-bonding network present between β-strands in the fibril[23,31]. This indicates that the change in cross-sectional diameter is associated with a change in the chemical environment, and therefore the tertiary/quaternary structure of the fibrils under investigation. Such changes in tertiary/quaternary structure of fibrils are associated to an increase in their size, of their surface to volume ratio and reduced seeding capability. As in the case of Aβ42, where fibrils can act as further templates for seeding and accelerate the aggregation process[6,32], this change in fibril size and structure may explain the variability in seeding capacity described above. The slight decrease in seeding capacity is consistent with the decrease in available fibril surface area to act as a template for further monomer misfolding and aggregation, or may be associated with fibril-fibril association processes that can mask specific nucleation sites for seeding the aggregation of Aβ monomers. It is not yet possible to disentangle if the different seeding capability arises mainly from the different size and surface-to-volume ratio or from their intrinsic differences in secondary structure. Further real-time studies of nucleation, elongation and other molecular events are warranted to uncover the fundamental relationship between fibril surface-to-volume ratio to their seeding mechanisms[33,34].

Conclusions

We have characterised the morphology, size, chemical and structural properties of fibrillar aggregates of Aβ42 within the plateau phase in in vitro aggregation reactions. We have identified that within this phase, fibrils undergo a maturation process leading to an increase in their cross-sectional diameter (thickness) and length, causing a decrease of their density in solution, as well as a change in the fibril hydrogen-bonding network and secondary structure. Such changes in morphology and secondary structure are associated with a variable seeding capacity.

These results shed light on the dynamic processes occurring in the plateau phase of aggregation, contributing to our understanding of the behaviour of mature fibrils. A better understanding of the microscopic processes that take place in the plateau phase increase our knowledge of the protein aggregation process. This also helps the development of procedures to handle amyloid fibrils for diverse applications, from drug discovery to materials science, where knowledge of fibril properties can be used to inform and tailor their use in medical assays or for the development of protein-based sustainable materials[35,36].

Methods

Aβ42 production. Expression and purification of the recombinant Aβ (M1-42) peptide (MDAEFRHDSGYEVHHQKLVF-FAEDVGSNKGAIIGLMVGGVVIA), denoted Aβ42, were carried out as previously described[37]. We note that studies comparing native Aβ(1-42) and Aβ (M1-42) have found no significant difference in aggregation rates, mechanisms, and fibril structure[38]. Aβ42 was expressed in the *Escherichia coli* BL21Gold (DE3) strain (Stratagene, La Jolla, CA) and purified by sonication and dissolving the inclusion bodies in 8 M urea, followed by ion exchange in batch mode on diethylaminoethyl cellulose resin. Fractions containing Aβ42 were lyophilised and further purified using a Superdex 75 HR 26/60 column (GE Healthcare, Chicago, IL), and eluates were analyzed using SDS−polyacrylamide gel electrophoresis for the presence of the desired protein product. The fractions containing the recombinant peptides were combined, frozen using liquid nitrogen, and lyophilised in 20 mM sodium phosphate buffer, pH 8, 0.2 mM EDTA. The lyophilised products were then stored at −80 °C.

Chemical kinetics. Solutions of monomeric peptides were prepared by dissolving the lyophilized Aβ42 peptide in 6 M GuHCl. Monomeric forms were purified from potential oligomeric species and salt using a Superdex 75 10/300 GL column (GE Healthcare) at a flow rate of 0.5 mL·min^{-1}, and were eluted in 20 mM sodium phosphate buffer (pH 8) supplemented with 200 μM EDTA. The center of the peak was collected, and the peptide concentration was determined from the absorbance of the integrated peak area using $\varepsilon_{280} = 1490$ L·mol^{-1}·cm^{-1}. The obtained monomer was diluted with buffer to the desired concentration and supplemented with 20 μM ThT from a 1 mM stock. All samples were prepared in low-binding Eppendorf tubes on ice using careful pipetting to avoid introduction of air bubbles. Each sample was then pipetted into multiple wells of a 96-well half-area, low-binding, clear-bottomed PEG coating plate (Corning 3881), at 80 μL per well.

Seeding assays. For the seeded experiments, preformed fibrils were freshly prepared just before the experiment without sonication because it has been shown previously that sonicating the fibrils for 10 min in a sonicator bath to delump the fibrils has no effect on their capacity to accelerate secondary nucleation[15]. ThT experiments were set up just as above for 5 μM Aβ42 samples in 20 mM sodium phosphate buffer (pH 8) with 200 μM EDTA, and 20 μM ThT. The ThT fluorescence was monitored for 3.5 h to verify the formation of fibrils. Samples were then collected from the wells into low-binding tubes with consistent thorough mixing and pipetting. The plate was then inserted back into the platereader until the time reached for collecting fibrils at a later plateau phase. We note a signal change in ThT during the initial period of reinserting the plate (Fig. 3a), which is attributed to the sample temperature equilibrating within the plate reader, resulting in fluorescence efficiency changes[39].

The final concentration of fibrils, in monomer equivalents, was considered equal to the initial concentration of monomer. Fibrils were then added to freshly prepared monomer to reach a 0.5%, 1%, 5%, or 10% final concentration of seeds.

AFM imaging. High-resolution and phase-controlled AFM was performed on positive functionalized mica substrates[21]. 10 μL of 0.5% (v/v) 3-aminopropyl-triethoxysilane (APTES, Sigma) in Milli-Q water was deposited onto freshly cleaved mica and incubated for 1 min. The substrate was rinsed three times with 1 mL of Milli-Q water and dried by a gentle stream of nitrogen gas. Finally, for each sample, an aliquot of 10 μL of the solution was deposited on the functionalized surface. The droplet was incubated for 5 min, then rinsed with 1 mL of Milli-Q water and dried under nitrogen gas. The preparation was carried out at room temperature. AFM maps were acquired using an NX10 AFM (Park Systems) operating in non-contact mode and equipped with a silicon tip (PPP-NCHR, 42 N/m) with a nominal radius <10 nm.

Image flattening and single-molecule size analysis was performed by SPIP (Image Metrology) software. Statistical analysis of fibril height and length was performed using Origin Pro (X), using a paired *t*-test. Particles volume was measured using Gwyddion, by considering the integral of the sample height over the covered area[40].

Fabrication of microfluidic spray devices. A two-step photo-lithographic process was used to fabricate the master used for casting microfluidic spray devices. In brief, a 25 µm thick structure was fabricated (3025, MicroChem) was spin-coated onto a silicon wafer. This, was then soft-baked for 15 min at 95 °C. An appropriate mask was placed onto the wafer, exposed under ultraviolet light to induce polymerization, and then post-baked at 95 °C. A second 50 µm thick layer (SU-8 3050, MicroChem) was then spin-coated onto the wafer and soft-baked for 15 min at 95 °C. A second mask was then aligned with respect to the structures formed from the first mask, and the same procedure was followed, i.e., exposure to UV light and post-baking for 15 min at 95 °C. Finally, the master was developed in propylene glycol methyl ether acetate (Sigma-Aldrich) to remove any photoresist which had not cross-linked.

A 1:10 ratio of PDMS curing agent to elastomer (SYLGARD 184, Dow Corning, Midland, MI) was used to fabricate microfluidic devices. The mixture was cured for 3 h at 65 °C. The hardened PDMS was cut and peeled off the master. The two complementary PDMS chips are then activated with O_2 plasma (Diener Electronic, Ebhausen, Germany) and put in contact with each other and aligned precisely such that the gas inlet intersects with the liquid inlet to form a 3D nozzle[13].

Use of microfluidic spray devices. Prior to introduction of sample, each device was tested and washed with MilliQ water for 5 min. Sample was then loaded into 200 µL air-tight glass syringes (Hamilton) and driven into the spray device using a syringe pump (Harvard apparatus). Solutions containing sample were pumped into the device with a flow rate of 100 µl/h, while the nitrogen gas inlet pressure was maintained at 3 bar. Deposition was conducted for a maximum of 15 s at a distance of 4.5 cm to ensure coalescence did not occur. Samples were sprayed directly onto the FTIR prism with no further washing steps required before measurements.

FTIR spectroscopy. Fibrils at 5 µM (monomer equivalent) were retrieved directly from an aggregation reaction and deposited onto the prism as described above. Measurements were performed on a Vertex 70 FTIR spectrometer (Bruker). Each spectrum was acquired with a scanner velocity of 20 kHz over 4000 to 400 cm^{-1} as an average of 200 scans using a *DiamondATR* unit and a deuterated lanthanum α-alanine-doped triglycine sulfate (DLaTGS) detector. New background spectra were acquired before each measurement. All spectra were analysed using OriginPro (Origin Labs). Spectra presented represent three individual spectra which were averaged and normalised. To determine the secondary structure composition of proteins, a second derivative analysis was performed. Spectra were first smoothed by applying a Savitzky-Golay filter.

Statistics and reproducibility. All chemical kinetics and FTIR experiments were performed in technical triplicates. For analysis of the AFM maps, at least five different maps at each time point were analysed; to study the difference between the aggregates, at least $n > 250$ aggregates were measured for each sample and time point.

Reporting summary. Further information on research design is available in the Nature Portfolio Reporting Summary linked to this article.

Data availability

The data generated or analysed in this study are included in the article and supporting information. The source data behind the graphs can be found in the Supplementary Data file.

References

1. Dobson, C. M., Knowles, T. P. J. & Vendruscolo, M. The Amyloid Phenomenon and Its Significance in Biology and Medicine. *Cold Spring Harb. Perspect. Biol.* https://doi.org/10.1101/cshperspect.a033878 (2019).
2. Arosio, P., Knowles, T. P. J. & Linse, S. On the lag phase in amyloid fibril formation. *Phys. Chem. Chem. Phys.* **17**, 7606–7618 (2015).
3. Knowles, T. P. J., Vendruscolo, M. & Dobson, C. M. The amyloid state and its association with protein misfolding diseases. *Nat. Rev. Mol. Cell Biol.* **15**, 384–396 (2014).
4. Knowles, T. P. J. et al. An analytical solution to the kinetics of breakable filament assembly. *Science* **326**, 1533–1537 (2009).
5. Hellstrand, E., Boland, B., Walsh, D. M. & Linse, S. Amyloid β-protein aggregation produces highly reproducible kinetic data and occurs by a two-phase process. *ACS Chem. Neurosci.* **1**, 13–18 (2010).
6. Cohen, S. I. A. et al. Proliferation of amyloid-β42 aggregates occurs through a secondary nucleation mechanism. *Proc. Natl Acad. Sci. USA* **110**, 9758–9763 (2013).
7. Michaels, T. C. T. et al. Chemical kinetics for bridging molecular mechanisms and macroscopic measurements of amyloid fibril formation. *Annu. Rev. Phys. Chem.* **69**, 273–298 (2018).
8. Fitzpatrick, A. W. P. et al. Atomic structure and hierarchical assembly of a cross-β amyloid fibril. *Proc. Natl Acad. Sci. USA* **110**, 5468–5473 (2013).
9. Lu, J. X. et al. XMolecular structure of β-amyloid fibrils in alzheimer's disease brain tissue. *Cell* **154**, 1257 (2013).
10. Yang, Y. et al. Cryo-EM structures of amyloid-b 42 filaments from human brains. *Science* **375**, 167–172 (2022).
11. Ruggeri, F. S., Šneideris, T., Vendruscolo, M. & Knowles, T. P. J. Atomic force microscopy for single molecule characterisation of protein aggregation. *Arch. Biochem. Biophys.* **664**, 134–148 (2019).
12. Ruggeri, F. S. et al. Microfluidic deposition for resolving single-molecule protein architecture and heterogeneity. *Nat. Commun.* **9**, 3890 (2018).
13. Kartanas, T. et al. Mechanism of droplet-formation in a supersonic microfluidic spray device. *Appl. Phys. Lett.* https://doi.org/10.1063/1.5145109 (2020).
14. Miller, A. et al. Enhanced surface nano-analytics of transient biomolecular processes. *Sci. Adv.* **9**, eabq3151 (2023).
15. Arosio, P., Cukalevski, R., Frohm, B., Knowles, T. P. J. & Linse, S. Quantification of the concentration of Aβ42 propagons during the lag phase by an amyloid chain reaction assay. *J. Am. Chem. Soc.* **136**, 219–225 (2014).
16. Lara, C., Adamcik, J., Jordens, S. & Mezzenga, R. General self-assembly mechanism converting hydrolyzed globular proteins into giant multistranded amyloid ribbons. *Biomacromolecules* **12**, 1868–1875 (2011).
17. Khurana, R. et al. A general model for amyloid fibril assembly based on morphological studies using atomic force microscopy. *Biophys. J.* **85**, 1135–1144 (2003).
18. Ruggeri, F. S. et al. Influence of the β-sheet content on the mechanical properties of aggregates during amyloid fibrillization. *Angew. Chem. Int. Ed.* **54**, 2462–2466 (2015).
19. Ruggeri, F. S. et al. Infrared nanospectroscopy characterization of oligomeric and fibrillar aggregates during amyloid formation. *Nat. Commun.* **6**, 1–9 (2015).
20. Ruggeri, F. S. et al. Identification and nanomechanical characterization of the fundamental single-strand protofilaments of amyloid α-synuclein fibrils. *Proc. Natl Acad. Sci. USA* **115**, 7230–7235 (2018).
21. Ruggeri, F. S. et al. Nanoscale studies link amyloid maturity with polyglutamine diseases onset. *Sci. Rep.* **6**, 1–11 (2016).
22. Vieweg, S. et al. The Nt17 domain and its helical conformation regulate the aggregation, cellular properties and neurotoxicity of mutant huntingtin exon 1. *J. Mol. Biol.* **433**, 167222 (2021).
23. Adamcik, J. et al. Evolution of conformation, nanomechanics, and infrared nanospectroscopy of single amyloid fibrils converting into microcrystals. *Adv. Sci.* **8**, 1–11 (2021).
24. Semerdzhiev, S. A., Dekker, D. R., Subramaniam, V. & Claessens, M. M. A. E. Self-assembly of protein fibrils into suprafibrillar aggregates: Bridging the nano- and mesoscale. *ACS Nano* **8**, 5543–5551 (2014).
25. Sidhu, A., Segers-Nolten, I., Raussens, V., Claessens, M. M. A. E. & Subramaniam, V. Distinct mechanisms determine α-synuclein fibril morphology during growth and maturation. *ACS Chem. Neurosci.* **8**, 538–547 (2017).
26. Ruggeri, F. S., Mannini, B., Schmid, R., Vendruscolo, M. & Knowles, T. P. J. Single molecule secondary structure determination of proteins through infrared absorption nanospectroscopy. *Nat. Commun.* **11**, 2945 (2020).

27. Ruggeri, F. S. et al. Infrared nanospectroscopy reveals the molecular interaction fingerprint of an aggregation inhibitor with single Aβ42 oligomers. *Nat. Comm.* **12**, 1–9 (2021).

28. Ruggeri, F. S. et al. The influence of pathogenic mutations in α-synuclein on kinetic mechanisms and structural characteristics of amyloid fibrils. *ACS Nano* **14**, 5213–5222 (2020).

29. Celej, M. S. et al. Toxic prefibrillar α-synuclein amyloid oligomers adopt a distinctive antiparallel β-sheet structure. *Biochem. J.* **443**, 719–726 (2012).

30. Natalello, A. et al. Conformational plasticity of the Gerstmann-Sträussler-Scheinker disease peptide as indicated by its multiple aggregation pathways. *J. Mol. Biol.* **381**, 1349–1361 (2008).

31. Ruggeri, F. S., Habchi, J., Cerreta, A. & Dietler, G. AFM-based single molecule techniques: unravelling the amyloid pathogenic species. *Curr. Pharm. Des.* **22**, 3950–3970 (2016).

32. Scheidt, T. et al. Secondary nucleation and elongation occur at different sites on Alzheimer's amyloid-b aggregates. *Sci. Adv.* **5**, eaau3112 (2019).

33. Zimmermann, M. R. et al. Mechanism of secondary nucleation at the single fibril level from direct observations of Aβ42 aggregation. *J. Am. Chem. Soc.* **143**, 16621–16629 (2021).

34. Thacker, D., Barghouth, M., Bless, M., Zhang, E. & Linse, S. Direct observation of secondary nucleation along the fibril surface of the amyloid β 42 peptide. *Proc. Natl Acad. Sci. USA* **120**, 1–9 (2023).

35. Wei, G. et al. Self-assembling peptide and protein amyloids: from structure to tailored function in nanotechnology. *Chem. Soc. Rev.* **46**, 4661–4708 (2017).

36. Mankar, S., Anoop, A., Sen, S. & Maji, S. K. Nanomaterials: amyloids reflect their brighter side. *Nano Rev.* **2**, 6032 (2011).

37. Johnny, H. et al. An anticancer drug suppresses the primary nucleation reaction that initiates the production of the toxic Aβ42 aggregates linked with Alzheimer's disease. *Sci. Adv.* **2**, e1501244 (2016).

38. Silvers, R. et al. Aggregation and fibril structure of Aβ(M01-42) and Aβ(1-42). *Biochemistry* **56**, 4850–4859 (2017).

39. Meisl, G. et al. Molecular mechanisms of protein aggregation from global fitting of kinetic models. *Nat. Protoc.* **11**, 252–272 (2016).

40. Nečas, D. & Klapetek, P. Gwyddion: an open-source software for SPM data analysis. *Cent. Eur. J. Phys.* **10**, 181–188 (2012).

Acknowledgements

Author contributions

A.M., S.C., E.K., and F.S.R. performed the experiments. A.M., S.C., and F.S.R. analysed the data. A.M. and F.S.R. wrote the original draft. A.M., S.C., E.K., T.P.J.K., M.V., and F.S.R. contributed to the final manuscript.

Competing interests

The authors declare no competing interests.

Additional information

Supplementary information The online version contains supplementary material available at https://doi.org/10.1038/s42003-024-05858-7.

Correspondence and requests for materials should be addressed to Tuomas P. J. Knowles, Michele Vendruscolo or Francesco Simone Ruggeri.

Reprints and permission information is available at http://www.nature.com/reprints

Publisher's note Springer Nature remains neutral with regard to jurisdictional claims in published maps and institutional affiliations.